

G.I. SYNGAYIVSKA, V.V. KOROTYEV

V.E. Lashkarev Institute of Semiconductor Physics, Department of Theoretical Physics,
Nat. Acad. of Sci. of Ukraine
(41, Nauky Ave., Kyiv 03028, Ukraine; e-mail: koroteev@ukr.net)**ELECTRICAL AND HIGH-FREQUENCY PROPERTIES
OF COMPENSATED GaN UNDER ELECTRON
STREAMING CONDITIONS**PACS 72.20.Ht, 72.20.Dp,
85.30.-z

Conditions required for the streaming effect and the optical-phonon transit-time resonance to take place in a compensated bulk GaN are analyzed in detail. Monte Carlo calculations of the high-frequency differential electron mobility are carried out. It is shown that the negative dynamic differential mobility can be realized in the terahertz frequency range, at low lattice temperatures of 30–77 K, and applied electric fields of 3–10 kV/cm. New manifestations of the streaming effect are revealed, namely, the anisotropy of the dynamic differential mobility and a specific behavior of the diffusion coefficient in the direction perpendicular to the applied electric field. The theory of terahertz radiation transmission through the structure with an epitaxial GaN layer is developed. Conditions for the amplification of electromagnetic waves in the frequency range of 0.5–2 THz are obtained. The polarization dependence of the radiation transmission coefficient through the structure in electric fields above 1 kV/cm is found.

Keywords: streaming, dynamic differential mobility, diffusion coefficient, Fröhlich constant, distribution function, transit-time frequency

1. Introduction

The study of the streaming effect in semiconductors was started in [1], where it was demonstrated that a special streaming regime of electron transport can be realized in polar semiconductors at low temperatures and in strong enough applied electric fields. This regime of electron transport is characterized by the emergence of a specific quasiballistic motion of electrons in the momentum space. In other words, under the influence of a strong electric field, electrons are accelerated to the energy of an optical phonon, $\hbar\omega_0$, almost without collisions. Having reached the energy $\epsilon_p \sim \hbar\omega_0$, the electron stops almost instantly and emits a polar optical phonon. Afterwards, a new cycle of acceleration begins. Such a cyclic motion of electrons results in the appearance of a strongly anisotropic streaming-like distribution function of electrons in the momentum space. The distribution function becomes strongly elongate along the electric field direction, being almost completely confined in the passive energy range, $\epsilon_p < \hbar\omega_0$.

For the electron streaming to be realized in semiconductor materials, a number of conditions should be satisfied.

(I) There must be $E^{(\text{str})} < E \ll E^{(\text{run})}$. On the one hand, the magnitudes of applied electric fields, E , must reach the values close to the characteristic streaming field $E^{(\text{str})} = p_0/e\langle\tau_p\rangle$, where p_0 is the electron momentum corresponding to the optical phonon energy, and $\langle\tau_p\rangle$ is the averaged time of the electron momentum relaxation in the passive energy range. On the other hand, the applied fields must be much lower than a certain characteristic field of the electron runaway effect, $E^{(\text{run})} = p_0/e\tau_0^+$, where τ_0^+ is the emission time of a polar optical phonon.

(II) For condition I to be satisfied, the mobility of electrons in low fields must be high enough, and, simultaneously, the interaction between electrons and optical phonons must be strong, $\langle\tau_p\rangle \gg \tau_0^+$.

(III) The lattice temperature T must be low, namely, $k_b T < \hbar\omega_0$, where k_b is the Boltzmann constant.

(IV) The electron concentration n_e must be low to avoid the electron–electron ($e - e$) scattering. At

least, the time of electron–electron collisions should exceed $\langle\tau_p\rangle$, $\tau_{e-e} > \langle\tau_p\rangle$.

The theoretical calculations of electric characteristics for hot electrons under streaming conditions meet difficulties in searching for a strongly nonequilibrium distribution function for charge carriers. The standard routine applied to the solution of the Boltzmann kinetic equation, which uses the expansion of the distribution function in a series of spherical harmonics [2, 3], is not effective, being too cumbersome, because the harmonics of high orders (higher than the second one) have to be taken into account. For the same reason, the conventional diffusion approximation [2] is unsuitable to describe the streaming. The electron temperature approximation [4] can be used only in the case of high electron concentrations, when the $e - e$ interaction is the dominating mechanism of scattering.

However, the approach proposed in [5] turned out to be rather fruitful and more adequate for the search of a strongly anisotropic distribution function. The Baraff method uses the approximation of a distribution function by the sum of isotropic and needle-shaped components. This method was widely applied in analytical researches of many types of problems dealing with the streaming effect [6–8]. Note that the Baraff method, in essence, gives rise to an approximate solution of the Boltzmann kinetic equation and provides the exact solution only in the limit of perfect streaming, when $E \gg E^{(\text{str})}$ and $\tau_0^+ = 0$.

Nowadays, the numerical methods got a wide popularity when being applied to the solution of the Boltzmann kinetic equation. The most effective of them is the Monte Carlo method. It enables the exact solution to be obtained for the Boltzmann kinetic equation in a wide range of electric fields [9, 10]. With the help of the Monte Carlo method, it was shown that the streaming-like distribution function of electrons can be formed in polar semiconductors in a dc electric field with the amplitude $E \sim E^{(\text{str})}$ [11–13].

Experimental confirmations of the formation of quasiballistic charge carrier motion in strong electric fields were obtained in the 1980s, when studying the current-voltage characteristics of submicronic diodes fabricated on the basis of pure GaAs, InAs, and InP [14, 15]. In those experiments, the oscillatory dependence of the static differential conductivity on the applied electric bias was observed at low enough (helium) temperatures, with the period of oscillations corresponding to the value of $\hbar\omega_0/e$. For $A^{\text{III}}B^{\text{V}}$ compounds, the oscillations of the static differential con-

ductivity were observed in strong magnetic fields as well [16].

Intensive researches of the streaming effect executed within the last decade involved a new class of wide-bandgap semiconductor materials, namely, group-III nitrides. Unique properties of nitride compounds [17] such as, in particular, a large energy of polar optical phonon, a large value of Fröhlich constant, and a relatively low effective mass (for GaN, those parameters are $\hbar\omega_0/k_b = 1000$ K, $\alpha_F = 0.4$, and $m^*/m_e = 0.2$, respectively) considerably improve the conditions for the streaming to take place. The Monte Carlo calculations carried out for GaN, InN, and AlN compounds [24–26] showed that the streaming-like distribution function of electrons emerges at temperatures of 10–150 K and in fields of 1–30 kV/cm. It was demonstrated that the drift velocity of electrons, V_d , and their average energy, $\langle\epsilon\rangle$, saturate in this interval of fields and approach the values $V_0/2$ ($V_0 = p_0/m^*$) and $\hbar\omega_0/3$, respectively.

Modern researches of the streaming effect in nitrides have a pronounced application aspect, namely, they are closely connected with the problem of developing the terahertz radiation sources. It was shown theoretically [18, 19] that the streaming regime can be accompanied by the emergence of a dynamic electric instability. This hypothesis was later confirmed experimentally for InP at helium temperatures [20]. The frequency dependence of the dynamic (high-frequency) mobility μ_ω in a system of streaming electrons has an oscillatory alternating-sign behavior. There exist the frequency intervals, in which $\text{Re}[\mu_\omega] < 0$. These frequency intervals are located near the characteristic *transit-time frequency* $\nu_R = eE/p_0$. The latter corresponds to the reciprocal electron acceleration time in the static field E until the polar optical phonon energy is reached. The appearance of the negative dynamic differential mobility is associated with the effect of electron bunching in the momentum space [21–23].

Driven by an ac electric field with the resonance frequency $\omega \sim 2\pi\nu_R$, the majority of electrons move in antiphase with the oscillations of this field, which results in the field strengthening. This effect is called the *optical phonon transit-time resonance* (OPTTR) effect or, shortly, the *transit-time resonance*. Its attractive feature consists in that the frequency and the amplitude of this resonance can be regulated by varying the strength of a dc electric field. This circumstance opens wide perspectives for the creation of high-frequency sources of new types.

Calculations of the dynamic differential mobility in doped bulk nitrides [27, 28] and high-quality nitride quantum wells [29, 30] showed that the dynamic negative differential mobility (DNNDM) can reach several hundreds of $\text{cm}^2/\text{V}/\text{s}$ in the frequency range from 0.5 to a few terahertz, in electric fields of 1–10 kV/cm, and within the temperature interval of 10–77 K. Similar conditions for the DNNDM in GaN quantum wells were obtained in works [31, 32]. Note, however, that the $e-e$ scattering was not taken into account in those calculations. The electron-electron coupling can change the conditions of existence for the DNNDM very much. For a GaN quantum well, it was shown [33] that the DNNDM amplitude substantially decreases already at the electron concentration $n_e = 10^{11} \text{ cm}^{-3}$ (the extrapolation of this value to the bulk sample gives the critical value of electron concentration $n_e = 10^{16} \div 10^{17} \text{ cm}^{-3}$). At high electron concentrations, when the $e-e$ scattering dominates, the DNNDM does not appear [34]. The negative influence of the electron-electron scattering can be avoided with the help of the compensation of free carriers. A high compensation degree allows the electron concentration to be reduced, hence making the electron-electron scattering not substantial. The case of compensated GaN was not discussed in detail in the literature. However, this case is important, because it provides better conditions for the streaming and transit-time resonance effects to be observed.

The main purpose of our researches was to reveal additional features in the electric characteristics of compensated GaN, which could definitely testify to the streaming emergence and could be identified in future experiments. In particular, we calculated, for the first time, the field dependence of the transverse diffusion coefficient and the frequency dependences of nonzero components of the dynamic mobility tensor in strong enough electric fields. It is of importance that those dependences can be observed in electro-gradient experiments and optical experiments dealing with the transmission of electromagnetic radiation with a given polarization through a structure that contains a layer of compensated GaN. For the calculations of stationary and high-frequency parameters of the electron gas in strong electric fields, the Monte Carlo numerical method was applied.

The paper is organized as follows. In Section 2, the model of electron transport is described. In Section 3, the features in the electron distribution function that emerges in a constant electric field are discussed, and the dependences of electric parameters

of the electron gas on the amplitude of an applied field are analyzed. In Section 4, the effect of transit-time resonance is studied, the spectra of the high-frequency mobility are presented for various relative orientations of dc and high-frequency electric fields, and the existence conditions for the DNNDM are analyzed. In Section 5, the theory of terahertz radiation transmission through a structure with a thin epitaxial GaN layer is developed. The main conclusions are summarized in Section 6.

2. Model of Electron Transport

Bulk GaN with a cubic modification and with the concentration of ionized impurities $N_i = 10^{16} \text{ cm}^{-3}$ is considered. The concentration of electrons is supposed to be $n_e < N_i$, i.e. the semiconductor is suggested to be compensated. The electron transport was simulated using the single-particle Monte Carlo method. The basic algorithms applied at the simulation were standard; they are described in detail in works [9, 10]. In our model, we considered the processes of electron scattering by acoustic and polar optical phonons, as well as by ionized impurities. The dispersion law for electrons was assumed to be parabolic, and all the processes of electron scattering were supposed to occur only near the bottom of the lowest Γ -valley. Explicit expressions for the probabilities of electron scattering by acoustic and polar optical phonons can be found in works [10, 35]. The electron scattering by ionized impurities was considered within the approach described in work [10]; it was found to be more correct for compensated semiconductors in comparison with the conventional Brooks–Herring and Conwell–Weisskopf models. This approach is described in Section 2.2.1 in more details.

2.1. Electron scattering by ionized impurities

As a rule, the electron scattering by ionized impurities is considered in the framework of either the Brooks–Herring (BH) or the Conwell–Weisskopf (CW) model. In these models, the screening of the field, which is induced by impurity ions, by conduction electrons is taken into account in different ways. In particular, the BH model uses the screened Coulomb potential

$$V(r) = \frac{Z_i e}{\kappa_0 r} \exp(-r/\lambda_D), \quad (1)$$

where $Z_i e$ is the charge of an impurity ion, κ_0 is the dielectric permittivity, $\lambda_D = (\kappa_0 k_b T / 4\pi e^2 n_e)^{1/2}$ is the Debye screening length, and n_e is the electron

concentration. In the CW model, the unscreened Coulomb potential is cut off at the distance $b = (3/4\pi N_i)^{1/3}$ between impurity ions, and the minimum scattering angle θ_{\min} for an electron with energy ϵ is determined by the formula

$$\text{ctg}\left(\frac{\theta_{\min}}{2}\right) = \frac{2\epsilon b \kappa_0}{e^2}. \quad (2)$$

Which of those models should be used depends on the ratio between λ_D and b . In a semiconductor with a high compensation degree ($n_e \ll N_i$), the inequality $\lambda_D \gg b$ is obeyed so that the CW model proves to be more adequate for applications. For a heavily doped semiconductor, in which all impurities are ionized ($N_i = n_e$), the inverse inequality $\lambda_D \ll b$ can be valid. In this case, the BH model is reasonable to be used.

In the cases where $\lambda_D \sim b$, it was suggested [10] to use the CW model with the screened Coulomb potential, rather than the ‘‘pure’’ one. In this model, the probability for an electron to transit from the initial state described by the wave vector \mathbf{k} into the state with the wave vector \mathbf{k}' within a unit time interval, provided that the electron is scattered by ionized impurities, is given by the expression

$$W_{\mathbf{k},\mathbf{k}'} = \frac{2^5 \pi^3 e^4 Z_i^2 N_i}{\hbar \kappa_0^2 \Omega} \left(\lambda_D^{-2} + (\mathbf{k}' - \mathbf{k})^2 \right)^{-2} \times \delta(\epsilon_{\mathbf{k}'} - \epsilon_{\mathbf{k}}), \quad (3)$$

where Ω is the normalization volume. In order to calculate the probability of the electron transition from the initial state into any other one within a unit time interval (the scattering rate), the quantity $W_{\mathbf{k},\mathbf{k}'}$ has to be multiplied by $\Omega/(2\pi)^3$, and the product has to be integrated over all \mathbf{k}' -values, bearing in mind that the angle θ between the vectors \mathbf{k} and \mathbf{k}' changes from θ_{\min} to π . For the parabolic dispersion law, we obtain the following formula describing the scattering rate for an electron with energy ϵ :

$$r_{\text{imp}} = \frac{2^{1/2} \pi Z_i^2 e^4 N_i}{\kappa_0^2 m^* 1/2 \epsilon^{1/2}} \left[\frac{1}{\epsilon_D + 4\epsilon \sin^2 \frac{\theta_{\min}}{2}} - \frac{1}{\epsilon_D + 4\epsilon} \right], \quad (4)$$

where $\epsilon_D = \hbar^2/2m^* \lambda_D^2$. Formula (4) gives the limiting transitions to the BH model as $\theta_{\min} \rightarrow 0$ and to the CW one as $\epsilon_D \rightarrow 0$.

In a compensated GaN with the concentration of ionized impurities $N_i = 10^{16} \text{ cm}^{-3}$, the concentration of electrons $n_e = 10^{15} \text{ cm}^{-3}$, and at a temperature of 30 K – below, it will be demonstrated that

these parameters are the best for the realization of the OPTTR – the values $b = 28 \text{ nm}$ and $\lambda_D = 35 \text{ nm}$ turn out close to each other so that it is formula (4) that should be used.

2.2. Total scattering rate

In our transport model, the total scattering rate is equal to the sum $r_{\text{tot}} = r_{\text{ac}} + r_{\text{imp}} + r_{\text{op}}$, where r_{imp} , r_{ac} , and r_{op} are the probabilities of the electron scattering by ionized impurities, acoustic phonons, and polar optical phonons, respectively. The probabilities $r_{\text{ac}} = r_{\text{ac}}^+ + r_{\text{ac}}^-$ and $r_{\text{op}} = r_{\text{op}}^+ + r_{\text{op}}^-$ take into account the emission (+) and absorption (–) processes of acoustic and polar optical phonons, respectively. Note that, within the actual temperature interval, the electron scattering by acoustic phonons is almost elastic so that $r_{\text{ac}}^+ \sim r_{\text{ac}}^-$. At the same time, the mechanism of electron scattering by polar optical phonons is essentially inelastic. Therefore, the relation between the probabilities r_{op}^+ and r_{op}^- strongly depends on the lattice temperature and the electron energy.

Figure 1 demonstrates the dependences of the total probability of electron scattering, r_{tot} , on the electron energy in bulk GaN with the concentration of ionized impurities $N_i = 10^{16} \text{ cm}^{-3}$ and the concentration of electrons $n_e = 10^{15} \text{ cm}^{-3}$ calculated for two lattice temperatures, $T = 30$ and 300 K. One can easily see a large difference between r_{tot} -values in the passive ($\epsilon < \hbar\omega_0$) and active ($\epsilon > \hbar\omega_0$) energy regions. It can be explained by the fact that the electrons with the energy $\epsilon < \hbar\omega_0$ are mostly scattered by ionized impurities and acoustic phonons, whereas the main scattering process for electrons with $\epsilon > \hbar\omega_0$ is driven by the more intensive spontaneous emission of polar optical phonons. For instance, for thermal electrons, i.e. electrons with the energy $\epsilon = 0.028 \times \hbar\omega_0$, the probabilities of their scattering by ionized impurities and acoustic phonons equal $r_{\text{imp}} = 1.6 \times 10^{12} \text{ s}^{-1}$ and $r_{\text{ac}} = 1.6 \times 10^{19} \text{ s}^{-1}$, respectively, at a lattice temperature of 30 K (curve 1 in Fig. 1). For an electron with the energy $\epsilon = 1.2 \times \hbar\omega_0$, the probability of the polar optical phonon emission is $r_{\text{op}}^+ = 4.5 \times 10^{13} \text{ s}^{-1}$, whereas $r_{\text{ac}} = 10^{11} \text{ s}^{-1}$ and $r_{\text{imp}} = 7.5 \times 10^{12} \text{ s}^{-1}$. At the same time, the polar optical phonon absorption is practically absent, $r_{\text{op}}^- \sim 10^2 \text{ s}^{-1}$.

At room temperature of the lattice, $T = 300 \text{ K}$ (curve 2 in Fig. 1), the value of r_{tot} for electrons with the energy $\epsilon < \hbar\omega_0$ turns out several times larger owing mainly to the growth of the role of inelastic processes in the optical phonon absorption. For example, for electrons with the energy $\epsilon = 0.28 \times \hbar\omega_0$,

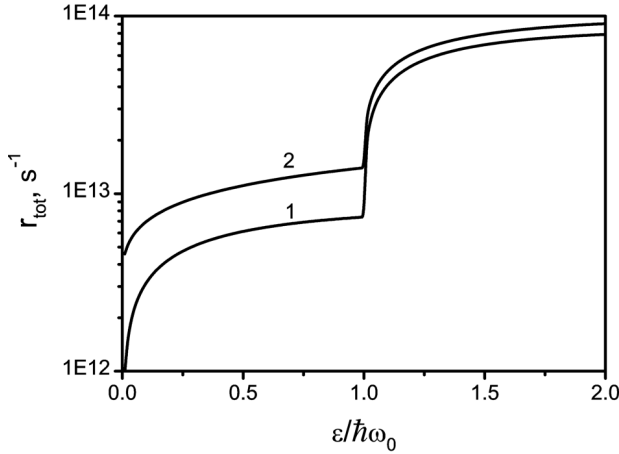


Fig. 1. Dependences of the total electron scattering rate on the electron energy at the temperature $T = 30$ (1) and 300 K (2)

we have $r_{\text{imp}} = 5.5 \times 10^{12} \text{ s}^{-1}$, $r_{\text{ac}} = 5.1 \times 10^{11} \text{ s}^{-1}$, and $r_{\text{op}}^- = 3.3 \times 10^{12} \text{ s}^{-1}$. At the same time, for an electron with the energy in the active range, $\epsilon = 1.2 \times \hbar\omega_0$, we have $r_{\text{ac}} = 10^{12} \text{ s}^{-1}$, $r_{\text{imp}} = 10^{13} \text{ s}^{-1}$, $r_{\text{op}}^- = 3 \times 10^{12} \text{ s}^{-1}$, and $r_{\text{op}}^+ = 4.5 \times 10^{13} \text{ s}^{-1}$.

The dependence of r_{tot} on the electron energy, which was described above, is inherent to all nitrides. Note that the larger the difference between the r_{tot} -values in the active and passive energy ranges, the more favorable are the conditions for the emergence of the streaming effect.

3. Steady-State Electron Characteristics

In the streaming regime, the electron motion becomes quasiperiodic, which finds its reflection in the distribution function of electrons and in the transport characteristics of the electron gas. The qualitative estimation of the characteristic electric field $E^{(\text{str})}$, in which the streaming regime is realized, can be done on the basis of low-field mobility values for electrons. Therefore, instead of immediately proceeding to the analysis of stationary electron parameters, it is reasonable to discuss the dependence of the low-field electron mobility on the lattice temperature in detail.

3.1. Low-field electron mobility

At low temperatures ($k_{\text{b}}T < \hbar\omega_0$), when only the elastic mechanisms of scattering are actual, the electron mobility can be calculated analytically with the use of the τ -approximation, namely,

$$\mu_0 = \frac{e}{m^*} \langle \tau_p \rangle, \quad (5)$$

where

$$\langle \tau_p \rangle = \frac{4}{3\sqrt{\pi}(k_{\text{B}}T)^{5/2}} \int_0^{\infty} d\epsilon \epsilon^{3/2} r_p^{-1}(\epsilon) \exp\left(-\frac{\epsilon}{k_{\text{B}}T}\right) \quad (6)$$

is the statistically averaged momentum relaxation time. Here, r_p is the inverse time of momentum relaxation. According to Matthiessen's rule,

$$r_p = r_{p,\text{ac}} + r_{p,\text{imp}}, \quad (7)$$

where $r_{p,\text{ac}}$ and $r_{p,\text{imp}}$ are the inverse momentum relaxation time at acoustic phonons and ionized impurities, respectively. The explicit expressions for $r_{p,\text{ac}}$ and $r_{p,\text{imp}}$ can be found in many manuals (see, e.g., textbook [36]). If the process of scattering by ionized impurities is examined in the framework of the Conwell–Weisskopf model with screened Coulomb potential, the following formula has to be used for the calculation of $r_{p,\text{imp}}$:

$$r_{p,\text{imp}} = \frac{\pi Z_i^2 e^4 N_i}{\kappa_0^2 \sqrt{2m^*}} \frac{1}{\epsilon^{3/2}} \left[\log \left(\frac{\epsilon_{\text{D}} + 4\epsilon}{\epsilon_{\text{D}} + 4\epsilon \sin^2 \frac{\theta_{\text{min}}}{2}} \right) - \frac{4\epsilon_{\text{D}}(1 - \sin^2 \frac{\theta_{\text{min}}}{2})}{(\epsilon_{\text{D}} + 4\epsilon)(\epsilon_{\text{D}} + 4\epsilon \sin^2 \frac{\theta_{\text{min}}}{2})} \right]. \quad (8)$$

The dependence of $r_{p,\text{imp}}$ on the electron energy ϵ is shown in the inset in Fig. 2. At high energies, the value of $r_{p,\text{imp}}$ decreases with the growth of ϵ as $\epsilon^{-3/2}$. Such a behavior of $r_{p,\text{imp}}$ is explained by the fact that faster electrons are mainly scattered at small angles. For the sake of comparison, the probability of the electron scattering by ionized impurities r_{imp} grows with the electron energy (see Fig. 1).

Note that, at high temperatures, when the role of the inelastic scattering mechanisms becomes essential, the τ -approximation loses its meaning, so that expression (5) cannot be used. For the exact calculation of the electron mobility in a low field, μ_0 , in a wide temperature range, either of the following procedures can be applied: (1) the Monte Carlo method is used to calculate the dependence of electron drift velocity V_{dr} in the field with strength E ; afterwards, the electron mobility can be determined from the slope of the curve $V_{\text{dr}}(E)$ [37]; or (2) the Monte Carlo method is used to calculate the diffusion coefficient D_0 ; afterwards, the electron mobility can be determined from the Einstein relation $\mu_0 = eD_0/k_{\text{b}}T$ [38]. In the case of low fields, the second way turns out to be more accurate and less dependent on the statistical noise

produced by the Monte Carlo calculations. Therefore, it was the second way that was selected by us to calculate the dependence of the electron mobility in low fields on the lattice temperature.

As is seen from Fig. 2, the dependence of the low-field mobility μ_0 on T is nonmonotonous. In the temperature interval 30–120 K, the μ_0 -values increase with T , because electrons are mainly scattered by acoustic phonons and ionized impurities, with the latter process dominating. It is of interest that the growth of μ_0 at higher T is associated with the decreasing dependence of $r_{p,imp}$ on the energy. As the lattice temperature increases, the fraction of high-energy electrons, for which scattering by ionized impurities is less intensive, grows. In Fig. 2, the results of calculations of the low-field mobility carried out either in the framework of the Monte Carlo method or with the use of formulas (5)–(8) are evidently identical within the temperature interval $T = 30 - 120$ K. Starting from a temperature of 120 K, the electron mobility μ_0 diminishes with the growth of T , which is connected with the enhancement of the role of the mechanisms of scattering by acoustic and polar optical phonons. If the temperature continues to grow, the role of the electron scattering by polar optical phonons increases considerably. In Fig. 2, this fact is illustrated by an increasing discrepancy between the exact mobility value obtained by the Monte Carlo method and its approximation calculated by formulas (5)–(8). At room temperature, the mobility of electrons is mainly governed by their scattering by polar optical phonons. The values calculated by us are close to those measured in high-quality GaN epitaxial layers grown up on Al_2O_3 substrates [39].

At $T = 30$ K, the electron mobility equals $5000 \text{ cm}^2/\text{V}\cdot\text{s}$ so that the characteristic electric field of the streaming is $E^{\text{str}} = 8 \text{ kV}/\text{cm}$; whereas the electron mobility at $T = 77$ K is close to $10000 \text{ cm}^2/\text{V}\cdot\text{s}$, and $E^{\text{str}} = 4 \text{ kV}/\text{cm}$.

3.2. Electron distribution function

Generally speaking, the distribution function of electrons in a bulk semiconductor is a function of three momentum variables, $F(p_x, p_y, p_z)$. However, the distribution function of electrons in a uniform dc electric field has the axial symmetry with respect to the field direction. Hence, if an electric field directed along the z -axis is applied to the semiconductor, it is enough to analyze the distribution functions of electrons in the momentum space in two directions, namely, along the

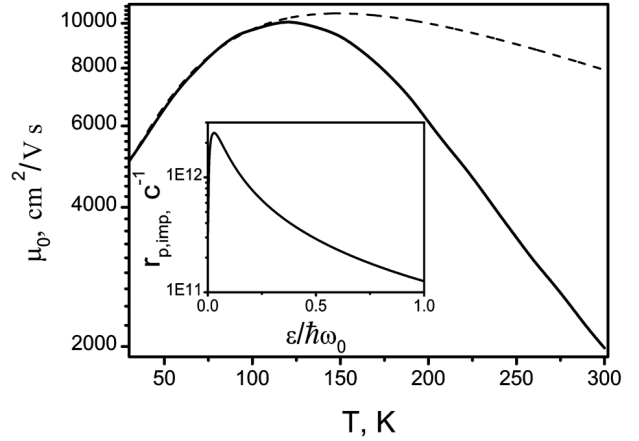


Fig. 2. Dependences of the low-field electron mobility on the lattice temperature calculated exactly by the Monte Carlo method (solid curve) and approximately by formulas (5)–(8) (dashed curve). $N_i = 10^{16} \text{ cm}^{-3}$ and $n_e = 10^{15} \text{ cm}^{-3}$

field, $f(p_z)$, and across it, $f(p_x)$. The distribution functions $f(p_z)$ and $f(p_x)$ are introduced as follows:

$$f(p_z) = \int \int dp_x dp_y F(p_x, p_y, p_z) / N$$

and

$$f(p_x) = \int \int dp_z dp_y F(p_x, p_y, p_z) / N,$$

where

$$N = \int \int \int dp_x dp_y dp_z F(p_x, p_y, p_z)$$

is the normalization integral.

The calculated distributions of electrons in the momentum space along and across the applied electric field are shown in Fig. 3 (panels *a* and *b*, respectively). Already in a field of $0.5 \text{ kV}/\text{cm}$, the system of electrons becomes nonequilibrium, and the difference between the electron distributions along and across the electric field is well distinguished. The distribution of electrons along the electric field has an appreciable asymmetry, which is associated with the existence of two groups of electrons, namely, low-energy electrons, which are isotropically distributed in the space of their momenta, and high-energy ones with the momenta directed along the electric field. As the electric field grows, the number of such monodirected electrons increases, and the electron distribution becomes more and more anisotropic. In the perfect streaming limit, all electrons have their momenta directed along the field, and the distribution function of electrons

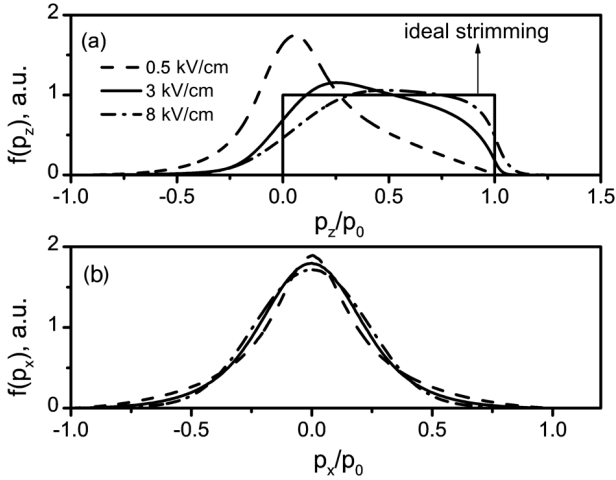


Fig. 3. Distributions of electrons in the momentum space (a) along and (b) across the electric field in GaN. $N_i = 10^{16} \text{ cm}^{-3}$, $n_e = 10^{15} \text{ cm}^{-3}$, and $T = 30 \text{ K}$

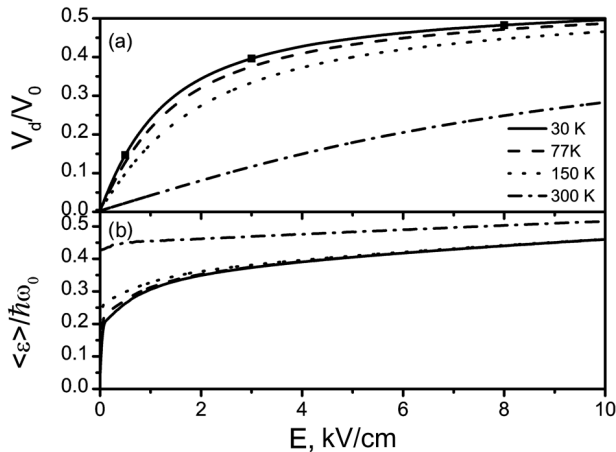


Fig. 4. Dependences of (a) drift velocity and (b) average energy of electrons on the electric field amplitude. $V_0 = 4 \times 10^7 \text{ cm/s}$ is the characteristic velocity. The other parameters of the material are the same as in Fig. 3. Points correspond to the field values, at which the distribution functions depicted in Fig. 3 were calculated

along the field has a step-like shape. From Fig. 3,a, it is evident that, for the fields of 3–8 kV/cm, the shape of the electron distribution function along the field is close to the step-like one. At the same time, the distribution function of electrons across the field, $f(p_x)$, remains symmetric. In the directions perpendicular to the field, the dominating fraction of electrons have momenta $p_x, p_y < p_0$. For the growing field, one can observe a weak compression of tails of the transverse component of the distribution function $f(p_x)$ (see Fig. 3,b).

In the fields higher than 10 kV/cm, the streaming effect becomes destroyed, because electrons penetrate deeper into the active energy range.

3.3. Steady-state electric characteristics

The streaming regime can manifest itself through the emergence of characteristic features in the dependences of stationary electric parameters on the applied field. Among those, there are weak dependences of the drift velocity V_d and the average energy $\langle \epsilon \rangle$ on the applied electric field strength E . In Fig. 4, one can easily see that, in the range of low, i.e. pre-streaming, electric fields 0.1–1 kV/cm, the dependence of the drift velocity on the field is approximately linear, but becomes sublinear if the field continues to grow. In the fields 3–10 kV/cm, the streaming type of electron transport is formed: the drift velocity practically does not change as the field grows, being close to $V_0/2$, which corresponds to the drift velocity in the perfect streaming model. A similar scenario is observed for the field dependence of the average energy. In the developed streaming regime, the value of $\langle \epsilon \rangle(E)$ approaches that of $\hbar\omega_0/3$, which is characteristic of the perfect streaming limit. It is worth noting that the dependences $V_d(E)$ and $\langle \epsilon \rangle(E)$ qualitatively do not differ strongly from each other within the temperature interval 30–150 K.

At room temperature, the situation is different. The streaming regime does not emerge owing to the presence of the strongly inelastic scattering in the passive energy range, the mechanism of which consists in the absorption of a polar optical phonon. In the fields 3–10 kV/cm, the dependence of the drift velocity on the field remains almost linear, the average energy almost does not change and remains close to the equilibrium value $3/2 \times k_b T$.

The emergence of the streaming regime can also be clearly traced by detecting a nonmonotonous field dependence of the transverse component of the average electron energy, $\langle \epsilon_{\perp} \rangle = \langle (p_x^2 + p_y^2)/2m^* \rangle$, where p_x and p_y are the electron momenta in the directions perpendicular to the field. In Fig. 5, the field dependences of $\langle \epsilon_{\perp} \rangle$ calculated for various lattice temperatures are depicted. At cryogenic temperatures and in low fields (less than 1 kV/cm), the value of $\langle \epsilon_{\perp} \rangle$ grows owing to the heating of the electron gas, which mainly manifests itself in the isotropic broadening of the electron distribution function in the momentum space. If the field amplitude increases further, $\langle \epsilon_{\perp} \rangle$ decreases and saturates in fields that correspond to

the developed streaming, which is associated with the narrowing of high-energy tails of the electron distribution function in the directions perpendicular to the field (see Fig. 3,*b*). At room temperature, both $\langle \epsilon_{\perp} \rangle$ and the total average energy $\langle \epsilon \rangle$ practically do not change as the field grows.

Another attribute of the fact that the electron transport in the streaming regime consists in a specific behavior of the field dependence of the electron diffusion coefficient in the coordinate space. As was shown above, the electron distribution function across the field gets narrowed at the streaming formation. As a result, the diffusion motion of electrons across the field must be inhibited, which would lead to a reduction of the diffusion coefficient D_{\perp} in the direction perpendicular to the field. This feature was discussed in work [31], when analyzing the streaming effect for the two-dimensional electron gas in the framework of the Baraff approximation. For today, a lot of researches have been carried out concerning the diffusion coefficient in bulk nitride samples [42] in strong fields (up to 0.5 MV/cm). At the same time, the interval of moderate electric fields, at which the streaming effect becomes possible, was not given a proper attention.

In Fig. 6, the field dependences $D_{\perp}(E)$ calculated for various lattice temperatures by the Monte Carlo method are shown. In heating fields of 0–0.25 kV/cm and at cryogenic lattice temperatures, the magnitude of D_{\perp} drastically grows. If the field amplitude grows further and the streaming-like distribution of electrons is formed, the value of D_{\perp} decreases. Starting from a field of 3 kV/cm, i.e. in the developed streaming regime, D_{\perp} saturates and approached values of 20–25 cm²/s, which are close to or even lower than the values for the equilibrium diffusion coefficients—the corresponding values are 13, 57, and 120 cm²/s at lattice temperatures of 30, 77, and 150 K, respectively. At room temperature, D_{\perp} is almost independent of the field amplitude, varying from 50 cm²/s in the zero field to 30 cm²/s in a field of 10 kV/cm.

Thus, a number of features in the field dependences of electric parameters, which point to the emergence of the streaming effect, are observed for the electron gas in a compensated bulk GaN with the concentration of ionized impurities $N_i = 10^{16}$ cm⁻³, the electron concentration $n_e = 10^{15}$ cm⁻³, in the fields of a few kV/cm, and at lattice temperatures of 30–150 K. It is worth noting that the streaming regime can be identified according to the results of experimental measurements of the drift velocity and the

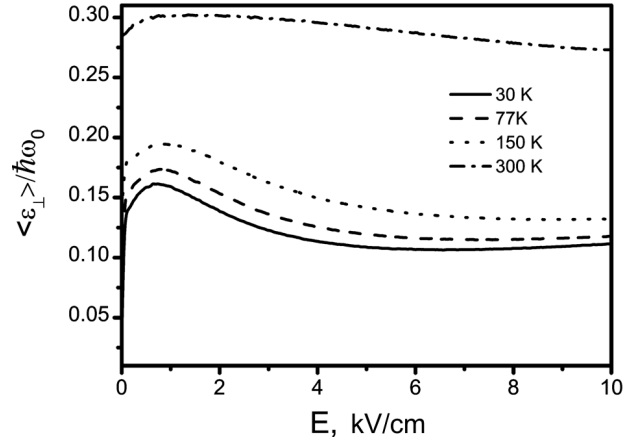


Fig. 5. Transverse component of the average electron energy as a function of the field

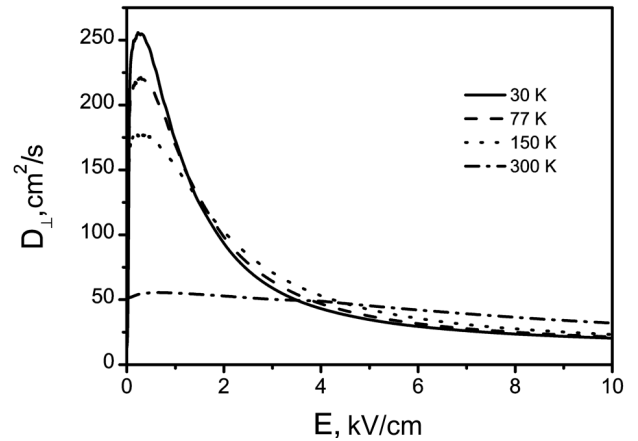


Fig. 6. Diffusion coefficient in the direction perpendicular to the field as a function of this field. The other parameters of the material are the same as in Fig. 3

diffusion coefficient of electrons in the direction perpendicular to the field.

4. High-Frequency Electric Characteristics

Surely, the most remarkable manifestation of the streaming phenomenon is the transit-time resonance effect, which is connected with the emergence of the negative dynamic differential conductivity as a response to an external high-frequency signal. In this section, we will discuss the spectra of the dynamic differential mobility (DDM), μ_{ω} , calculated by the Monte Carlo method using the single-particle algorithm [10, 44, 45]. We will analyze comprehensively the conditions of existence for the negative dynamic differential mobility (DNDDM) in a compensated GaN at various lattice temperatures and various relative

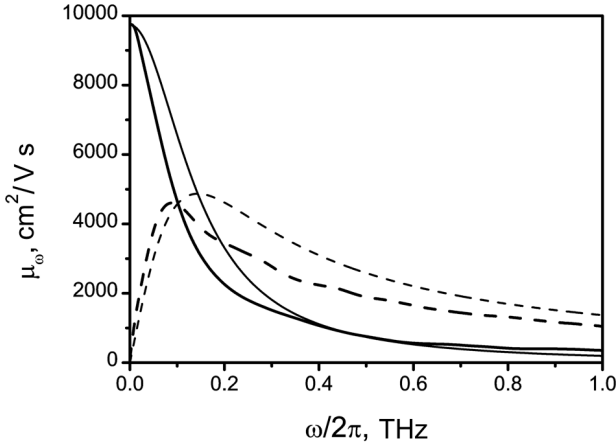


Fig. 7. Dependence of DDM on the frequency calculated in the framework of the Drude–Lorentz model (thin curves) and by the Monte Carlo method (bold curves). Solid curves correspond to $\text{Re}[\mu_\omega]$ and dashed ones to $\text{Im}[\mu_\omega]$. The dc field amplitude $E = 0.5$ kV/cm, $T = 30$ K, $N_i = 10^{16}$ cm $^{-3}$, and $n_e = 10^{15}$ cm $^{-3}$

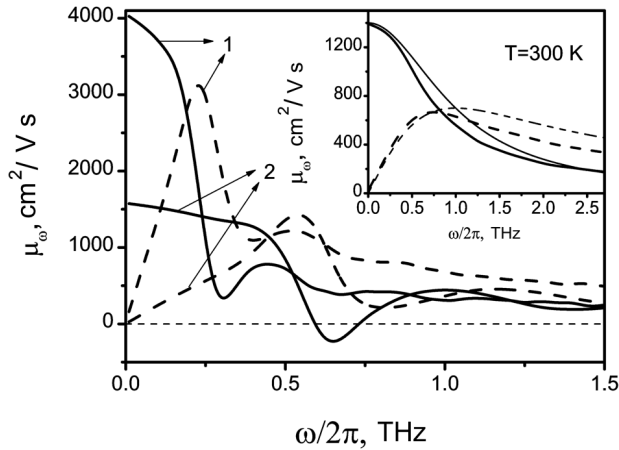


Fig. 8. Dependences $\text{Re}[\mu_\omega]$ (solid curves) and $\text{Im}[\mu_\omega]$ (dashed curves) at $T = 30$ K and $E = 1.5$ (1) and 3 kV/cm (2). The spectra $\text{Re}[\mu_\omega]$ and $\text{Im}[\mu_\omega]$ at $E = 3$ kV/cm and $T = 300$ K are shown in the inset

orientations of dc and ac electric fields. The analysis of μ_ω is started from the case where a dc field E and a low sinusoidal field with amplitude $E_\omega \ll E$, which are parallel to each other, are applied to the sample.

4.1. Dynamic differential mobility

In Fig. 7, the bold curves correspond to the frequency dependences of μ_ω calculated for the low stationary electric field $E = 0.5$ kV/cm using the Monte Carlo method. For comparison, the same dependences calculated in the framework of the Drude–

Lorentz model,

$$\mu_\omega = \mu_{0,E} / (1 - i\omega m^* \mu_{0,E} / e),$$

where $\mu_{0,E} = dV_d(E)/dE$ is the zero-frequency differential mobility, are also shown by thin curves. In the field $E = 0.5$ kV/cm, the electron distribution function still remains quasiisotropic, and, as is seen from Fig. 7, the shape of the μ_ω -spectrum is close to that of the Drude–Lorentz one.

If the dc field amplitude increases, the streaming regime starts to be formed, which manifests itself in the oscillatory dependence of the real and imaginary parts of DDM on the frequency. In Fig. 8, the μ_ω -spectra calculated for $E = 1.5$ and 3 kV/cm are depicted. Already at $E = 1.5$ kV/cm, the real part of DDM has a series of minima at the transit-time resonance frequency and its higher harmonics, but still remains positive. At $E = 3$ kV/cm, the real part of DDM changes its sign and becomes negative in a vicinity of the fundamental frequency of the transit-time resonance $\omega_{tr}/2\pi \approx 0.6$ THz. Note that, at room temperature and in the same electric field, the real and imaginary parts of DDM do not reveal any features, being well described by the Drude–Lorentz model. In the inset of Fig. 8, bold (calculation by the Monte Carlo method) and thin (the Drude–Lorentz model) curves are close to each other.

Hence, the amplitude and frequency windows of DNDM directly depend on the applied field magnitude and the temperature of a sample. In the frequency range, where $\text{Re}[\mu_\omega] < 0$, the amplification of a high-frequency signal occurs, which is proportional to the DNDM amplitude. Therefore, it is expedient to determine the intervals for temperatures and dc electric fields, at which the DNDM takes place and reaches minimum negative values.

4.2. Dependences of the OPTTR effect on the temperature and the field amplitude

In Fig. 9, the frequency dependences of $\text{Re}[\mu_\omega]$ are depicted only for the first actual resonance minimum. At higher-order minima, which are multiples of the transit-time frequency, the DNDM does not emerge. The most pronounced OPTTR effect is observed at a temperature of 30 K. The DNDM appears at $E \approx 2$ kV/cm and reaches a minimum value of -250 cm 2 /V/s in a vicinity of the frequency $\omega/2\pi \approx 0.64$ THz at $E \approx 3$ kV/cm. As the dc field amplitude increases, the frequency windows of the DNDM shift toward the high-frequency range and are

broaden out. At the same time, however, the DNNDM amplitude decreases. In Fig. 9, it is clearly seen that, at $T = 30$ K, the DNNDM appears in the field range within the limits 2–10 kV/cm and in the frequency interval from 0.38 to 2.5 THz (this interval is confined by a dash-dotted curve). However, if the field amplitude exceeds 10 kV/cm, a sufficient number of electrons can penetrate into the active range to violate the coherent motion of the majority of electrons, so that the DDM values become positive.

At $T = 77$ K, the frequency windows with the DNNDM still exist. However, the DNNDM manifests itself much weaker than at $T = 30$ K. The frequency interval, in which the DDM becomes negative, is much narrower at $T = 77$ K than at $T = 30$ K. At the fields within the interval 2.5–9 kV/cm, the DNNDM emerges at frequencies between approximately 0.56 and 2.2 THz. The largest DNNDM amplitude is realized at $E = 4$ kV/cm at a frequency of 0.9 THz and with the minimum $\text{Re}[\mu_\omega] \approx -100$ cm²/V/s.

At $T = 150$ K, the DDM also demonstrates the oscillatory dependence on the frequency; however, it does not become negative. It is of interest that, at this temperature, the low-field mobility $\mu_0 = 9500$ cm²/V/s (see Fig. 2), which is almost twice as large as that at $T = 30$ K ($\mu_0 = 5000$ cm²/V/s). Hence, the conditions for the streaming effect to take place seem to be better at $T = 150$ K rather than at $T = 30$ K, and, consequently, the OPTTR effect should have manifested itself more strongly just in the former case. However, the opposite situation is actually observed. Such a disagreement can be explained by the sensitivity of the OPTTR effect to the initial broadening of the equilibrium electron distribution function. For the distribution function with an anisotropy, which would be sufficient for the appearance of the DNNDM at $T = 150$ K, to be formed, a field stronger than that required at 30–77 K has to be applied to the semiconductor. However, in stronger fields, the DNNDM does not appear, because the penetration of electrons into the active energy range becomes substantial.

4.3. Anisotropy of dynamic differential mobility

In Section 4.2, the dependences of the real part of DDM on the frequency of the ac electric field and the amplitude of the dc one, which are parallel to each other, were discussed in detail. Under the streaming conditions, when the distribution function of elec-

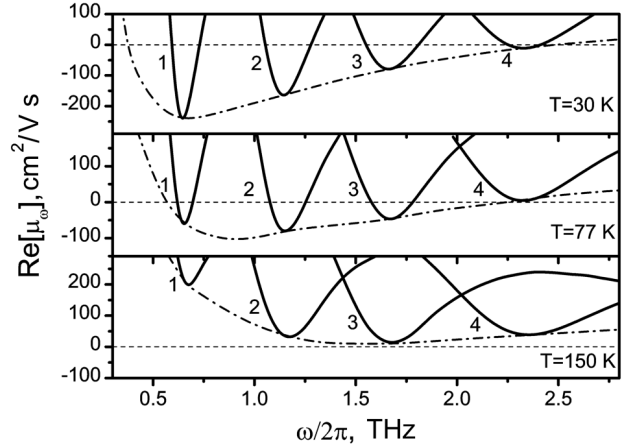


Fig. 9. $\text{Re}[\mu_\omega]$ -spectra in a vicinity of OPTTR frequencies at $E = 3$ (1), 5 (2), 7 (3), and 9 kV/cm (4). The dash-dotted curve is the envelope of $\text{Re}[\mu_\omega]$ -minima. $N_i = 10^{16}$ cm⁻³ and $n_e = 10^{15}$ cm⁻³

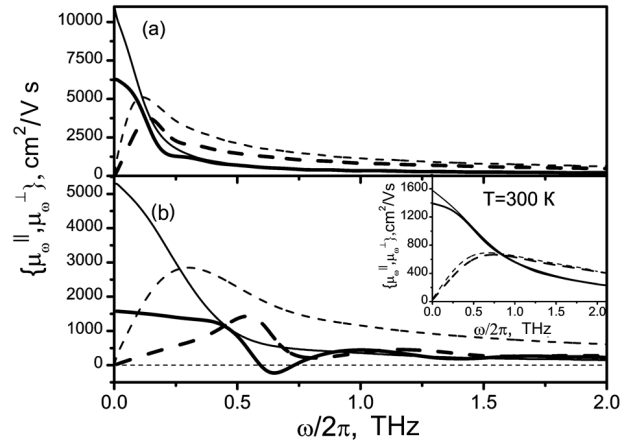


Fig. 10. Spectra of μ_ω^{\parallel} (bold curves) and μ_ω^{\perp} (thin curves) at $T = 30$ K and $E = 1$ (a) and 3 kV/cm (b). The real and imaginary parts of DDM are shown by solid and dashed, respectively, curves. The same spectra but at $T = 300$ K and $E = 3$ kV/cm are shown in the inset

trons is anisotropic, one may expect that the electron response should depend on the relative orientation of the dc field and the varying signal.

In Fig. 10, the dependences of DDM on the frequency of ac signals polarized in parallel and perpendicularly to the direction of the dc electric field are exhibited. The quantities μ_ω^{\parallel} and μ_ω^{\perp} describe the response of the electron system to the ac signal with the parallel and perpendicular, respectively, polarizations. At low frequencies, the μ_ω^{\parallel} - and μ_ω^{\perp} -values substantially differ from each other both in low fields (< 1 kV/cm), in which the distribution

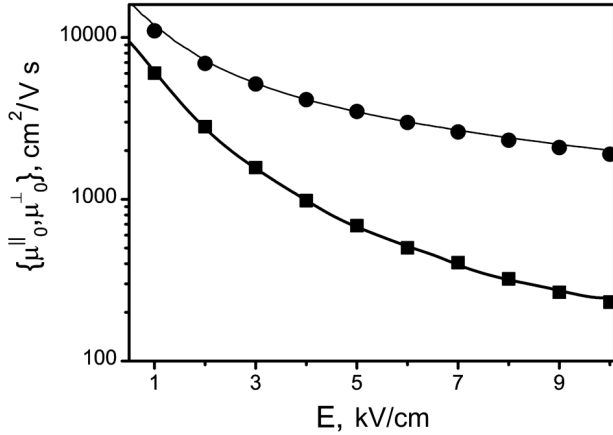


Fig. 11. Dependences μ_{ω}^{\parallel} (bold curves) and μ_{ω}^{\perp} (thin curves) calculated from stationary characteristics $V_d(E)$, $\langle\epsilon_{\perp}\rangle(E)$, and $D_{\perp}(E)$. μ_0^{\parallel} (squares) and μ_0^{\perp} (circles) values were calculated by the Monte Carlo method. The lattice temperature is 30 K

function of electrons is characterized by a moderate anisotropy, and in the developed streaming regime ($E = 3$ kV/cm).

The difference between μ_{ω}^{\parallel} and μ_{ω}^{\perp} survives even at the zero frequency, which is associated with the anisotropy of the electron distribution in the momentum space. In Fig. 11, the dependences of parallel, μ_0^{\parallel} , and perpendicular, μ_0^{\perp} , components of the differential mobility on the dc field strength E are shown. These dependences were obtained with the use of the Monte Carlo method, in which the μ_0^{\parallel} - and μ_0^{\perp} -values were calculated for an extremely low frequency. There is another approximate method for the determination of those quantities, which uses the values of stationary parameters. In a given dc field E , $\mu_0^{\parallel} \approx dV_d(E)/dE$. This relation is exact in the limit of low-signal response ($E_{\omega} \ll E$). To calculate μ_0^{\perp} , the generalized Einstein relation can be used,

$$\frac{D_{\perp}}{\mu_0^{\perp}} \approx \frac{\langle\epsilon_{\perp}\rangle}{e}, \quad (9)$$

with regard for the dependences $\langle\epsilon_{\perp}\rangle(E)$ (see Fig. 5) and $D_{\perp}(E)$ (see Fig. 6). The values calculated for μ_0^{\parallel} and μ_0^{\perp} by the Monte Carlo method coincide with the corresponding values obtained from the stationary characteristics $V_d(E)$, $\langle\epsilon_{\perp}\rangle(E)$, $D_{\perp}(E)$, and formula (9) (see Fig. 11). The fact that both determination methods bring about identical values for $\mu_0^{\perp}(E)$ can be explained by an almost Maxwellian distribution of electrons in the direction perpendicular to the dc field.

From Fig. 11, one can easily see that the dependence $\mu_0^{\parallel}(E)$ decreases more rapidly than the $\mu_0^{\perp}(E)$ one with the growth of the dc field amplitude. Such a behavior of $\mu_0^{\parallel}(E)$ can be explained by the fact that the sublinearity manifests itself much more strongly in the dependence $V_d(E)$, rather than in the $D_{\perp}(E)/\langle\epsilon_{\perp}\rangle(E)$ one. In fields of 3–8 kV/cm, which correspond to the developed streaming regime, a considerable difference between the $\mu_0^{\parallel}(E)$ - and $\mu_0^{\perp}(E)$ -values is retained. Hence, the experimentally observed substantial anisotropy of the differential mobility in strong electric fields can serve as an additional proof of the streaming formation.

In fields of 1–3 kV/cm, the distribution function of electrons in the momentum space remains symmetric in the direction perpendicular to the field. Consequently, the frequency dependence of μ_{ω}^{\perp} is well described by the Drude–Lorentz model and does not reveal an oscillatory behavior typical of μ_{ω}^{\parallel} (see Fig. 10). It is worth to note that there is no substantial difference between μ_{ω}^{\perp} - and μ_{ω}^{\parallel} -values in a dc field of 1 kV/cm, except for at very low frequencies. Under the streaming conditions (e.g., at 3 kV/cm), the response of the electron system in the parallel configuration of the fields E and E_{ω} differs cardinally from that in the perpendicular configuration. In the frequency interval, where μ_{ω}^{\parallel} becomes negative and μ_{ω}^{\perp} remains positive, an ac signal with the polarization perpendicular to the dc field, instead of being amplified, is effectively absorbed. This effect can be observed in optical experiments on the transmission of ultrahigh-frequency (terahertz) radiation through semiconductor structures. If a strong enough dc electric field is applied to a sample, the latter is characterized by the anisotropy of DDM and acts as a polarizer for a non-polarized beam. The efficiency of such a polarizer depends on the magnitude of applied dc electric field and the sample temperature. For instance, at $T = 300$ K, when the electron distribution function is still isotropic and the μ_{ω}^{\perp} - and μ_{ω}^{\parallel} -values practically coincide, the sample does not function as a polarizer.

Recently, the collaborators of the the Terahertz laboratory at the Montpellier University carried out an experiment, in which they tried to register the OPTTR effect and find the DNDM by detecting the amplification of terahertz radiation transmitted through a heterostructure with GaN [46]. Unfortunately, reliable confirmations for the OPTTR effect were not obtained. To elucidate what one could ex-

pect of such experiments, we developed a theory describing the light transmission through a sample with an active epitaxial layer of compensated GaN in the OPTTR regime.

5. Transmission of High-Frequency Radiation through a GaN Structure

In modern experiments, the complicated multilayered structures grown up on dielectric substrates are used. As a rule, the thickness of the active zone, a thin GaN layer, has an order of a few micrometers, which is much less than the wavelength λ_0 of terahertz electromagnetic radiation in vacuum. In similar structures, the thickness of dielectric substrate is much thicker than that of GaN layer, being, as a rule, of the same order of magnitude as λ_0 . In this section, we expound the theory of high-frequency radiation transmission through such structures. While studying the spectra of the transmission, reflection, and absorption coefficients for high-frequency radiation, the frequency dependences of DDM were applied, which were calculated with the use of the Monte Carlo method (see Section 4).

5.1. Theory of high-frequency radiation transmission through GaN

Let high-frequency radiation pass through a structure consisting of a dielectric substrate with the thickness d_s and the dielectric constant κ_s , covered with a delta-like GaN layer. The GaN layer is characterized by the two-dimensional complex conductivity $\sigma_\omega^* = \sigma'_\omega d + id(\sigma''_\omega - \kappa_0 \omega / 4\pi)$, where $\sigma'_\omega = en_e \text{Re}[\mu_\omega]$, $\sigma''_\omega = en_e \text{Im}[\mu_\omega]$, and d is the thickness of GaN layer. This expression takes the displacement current in the GaN layer into account. Let a plane wave $E_{p,\omega}(y) \exp(-i\omega t)$ with the amplitude $E_{p,\omega}(y)$ and the frequency ω fall normally on the structure surface. The electric field $E_{p,\omega}(y)$ of this wave satisfies the Maxwell equations,

$$\frac{d^2 E_{p,\omega}}{dy^2} + \begin{cases} \frac{\omega^2}{c^2} & y < 0 \\ \frac{\kappa_s \omega^2}{c^2} & 0 < y < d_s \\ \frac{\omega^2}{c^2} & y > d_s \end{cases} E_{p,\omega} = -\frac{4\pi i \omega \sigma_\omega^{*,p}}{c^2} E_{p,\omega} \delta(y), \quad (10)$$

where the subscript p specifies the wave polarization either along ($p = \parallel$) or across ($p = \perp$) the dc electric field. In Eqs. (10), the whole structure is supposed to be in vacuum. The solution of system (10) looks like

$$E_{p,\omega}(y) =$$

$$= \begin{cases} A_{p,\omega} \exp(ik_0 y) + B_{p,\omega} \exp(-ik_0 y), & y < 0, \\ C_{p,\omega} \exp(ik_s y) + D_{p,\omega} \exp(-ik_s y), & 0 < y < d_s, \\ F_{p,\omega} \exp(ik_0 y), & y > d_s, \end{cases} \quad (11)$$

where $k_0 = \omega/c$ and $k_s = \omega\sqrt{\kappa_s}/c$ are the wave numbers of plane waves in vacuum and the substrate, respectively. The coefficients $A_{p,\omega}$, $B_{p,\omega}$, $C_{p,\omega}$, $D_{p,\omega}$, and $F_{p,\omega}$ are determined from the following conditions at the coordinate planes $y = 0$ and $y = d_s$:

$$E_{p,\omega}(-0) = E_{p,\omega}(+0),$$

$$\frac{dE_{p,\omega}}{dy}(-0) - \frac{dE_{p,\omega}}{dy}(+0) = \frac{4\pi i \omega \sigma_\omega^{*,p}}{c^2} E_{p,\omega}(0),$$

$$E_{p,\omega}(d_s - 0) = E_{p,\omega}(d_s + 0),$$

$$\frac{dE_{p,\omega}}{dy}(d_s - 0) = \frac{dE_{p,\omega}}{dy}(d_s + 0). \quad (12)$$

After standard transformations, we obtain the following formulas for the transmission, $T_{p,\omega}$, and reflection, $R_{p,\omega}$, coefficients:

$$T_{p,\omega} = \left[\left(1 + \frac{\Gamma'_{p,\omega}}{2} \right)^2 + \frac{\Gamma''_{p,\omega}}{4} + \frac{(\kappa_s - 1)(\kappa_s - (1 + \Gamma'_{p,\omega})^2 - \Gamma''_{p,\omega})}{4\kappa_s} \times \sin^2(k_s d_s) - \frac{\sqrt{\kappa_s}(\kappa_s - 1)\Gamma''_{p,\omega}}{4\kappa_s} \sin(2k_s d_s) \right]^{-1}, \quad (13)$$

$$R_{p,\omega} = \left[\frac{\Gamma'_{p,\omega}}{4} + \frac{\Gamma''_{p,\omega}}{4} + \frac{(\kappa_s - 1)(\kappa_s - (1 - \Gamma'_{p,\omega})^2 - \Gamma''_{p,\omega})}{4\kappa_s} \sin^2(k_s d_s) - \frac{\sqrt{\kappa_s}(\kappa_s - 1)\Gamma''_{p,\omega}}{4\kappa_s} \sin(2k_s d_s) \right] \times T_{p,\omega}. \quad (14)$$

The absorption coefficient can be calculated by the formula $L_{p,\omega} = 1 - T_{p,\omega} - R_{p,\omega}$ or

$$L_{p,\omega} = \Gamma'_{p,\omega} \left(1 - \frac{\kappa_s - 1}{\kappa_s} \sin^2(k_s d_s) \right) \times T_{p,\omega}. \quad (15)$$

In all Eqs. (13)–(15), the notations $\Gamma'_{p,\omega} = 4\pi \text{Re}[\sigma_\omega^{*,p}]/c$ and $\Gamma''_{p,\omega} = 4\pi \text{Im}[\sigma_\omega^{*,p}]/c$ are used.

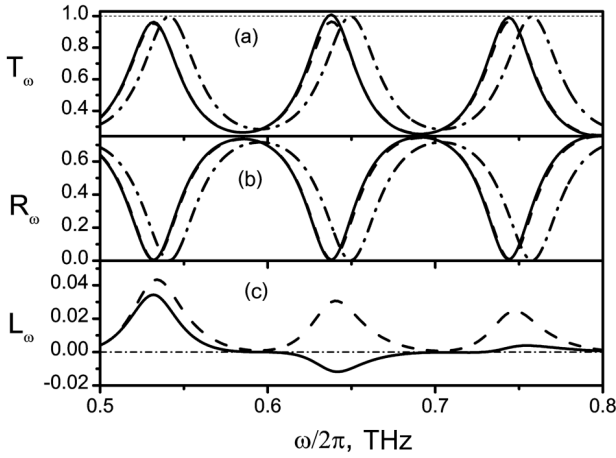


Fig. 12. Spectra of the (a) transmission, (b) reflection, and (c) absorption coefficients for the parallel (solid curves) and perpendicular (dashed curves) field configurations. T_{sub} , R_{sub} , and L_{sub} spectra are shown by dash-dotted curves. The parameters of the GaN layer are $N_i = 10^{16} \text{ cm}^{-3}$, $n_e = 10^{15} \text{ cm}^{-3}$, $d = 10^{-3} \text{ cm}$, $\kappa_0 = 8.9$, and $E = 3 \text{ kV/cm}$. The substrate (sapphire is supposed) parameters are $d_s = 0.04 \text{ cm}$ and $\kappa_s = 12$

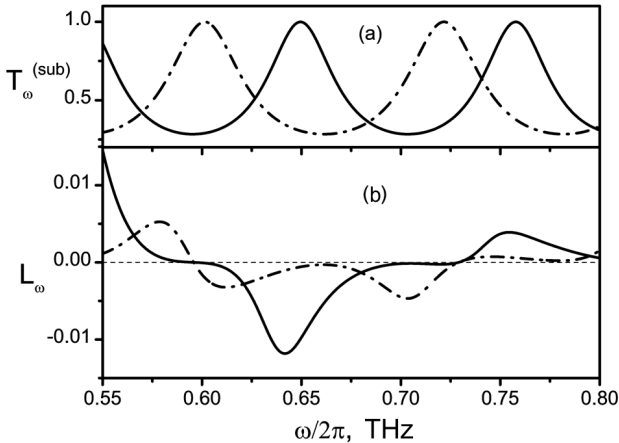


Fig. 13. (a) Transmission coefficient spectra for a single substrate and the (b) absorption coefficient spectra for the structure at $d_s = 0.036$ (dash-dotted curves) and 0.04 cm (solid curves). The other parameters of the material are the same as in Fig. 12

In the absence of a GaN layer, i.e. if there is only the substrate, the quantities $\Gamma'_{p,\omega}$ and $\Gamma''_{p,\omega}$ in formulas (13)–(15) equal zero, and the transmission, reflection, and absorption coefficients are determined in a standard way, as for a single dielectric wafer, namely,

$$T_{\text{sub}} = \frac{1}{1 + \frac{(\kappa_s - 1)^2}{4\kappa_s} \sin^2(k_2 d_s)},$$

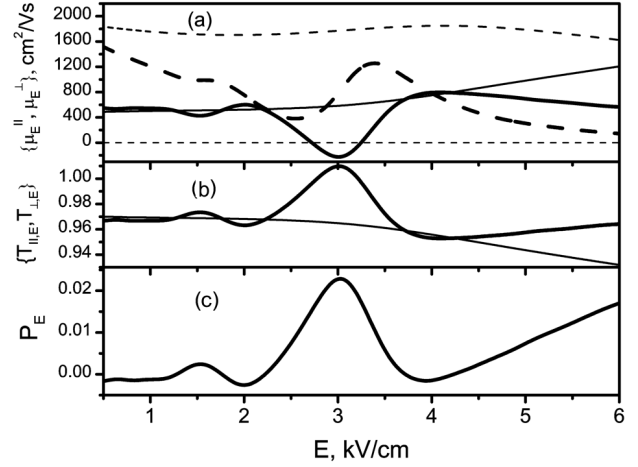


Fig. 14. Dependences of (a) the real (bold curves) and imaginary (thin curves) parts of μ_E^{\parallel} (solid curves) and μ_E^{\perp} (dashed curves), (b) the transmission coefficients along ($T_{\parallel,E}$, bold curve) and across ($T_{\perp,E}$, thin curve) the applied field, and (c) the polarization degree P_E on the field amplitude at a frequency of 0.64 THz . The parameters of the substrate and the active layer are the same as in Fig. 12

$$R_{\text{sub}} = 1 - T_{\text{sub}},$$

$$L_{\text{sub}} = 0. \quad (16)$$

5.2. Spectra of the transmission, reflection, and absorption coefficients

The transmission, reflection, and absorption coefficients for high-frequency radiation (Fig. 12) were calculated in such frequency intervals and at such values of dc electric field, when the DNDM manifests itself most strongly (Fig. 10,b). If an electromagnetic wave passes through a single substrate, then, for the given thickness and the dielectric constant of the latter, we obtain a set of frequencies ω_r ($r = 1, 2, 3, \dots$), which correspond to the Fabry–Perot modes of a plane-parallel dielectric wafer. Their values are given by the expression $\omega_r/2\pi = cr/(2d_s\sqrt{\kappa_s})$ and correspond to $T_{\text{sub}} = 1$. The presence of a thin active GaN layer with a low concentration of electrons on the substrate slightly modifies the transmission coefficient spectra of the system. The parameters of the substrate and the active element were so chosen that the DNDM frequency window should coincide with any of the frequencies ω_r . In the frequency interval $0.6\text{--}0.7 \text{ THz}$, the wave with the polarization along the dc field, when passing through the sample, becomes amplified. In this frequency interval, the absorption coefficient becomes negative and reaches a minimum

value of -1.5% at about 0.64 THz (Fig. 12). The negative absorption coefficient means that the sum of intensities for passed and reflected waves exceeds the incident wave intensity. Hence, we may say about the amplification of the electromagnetic field by the active element. For the sake of comparison, the coefficient of electromagnetic wave losses at this frequency under the wave reflection from a perfect silver mirror equals -0.5% . Therefore, the criterion of terahertz mode excitation in a resonator system composed of two plane-parallel metallic mirrors can be satisfied despite that the gain factor in the active layer is low.

For a wave with the polarization perpendicular to the dc field, the absorption coefficient is positive, and, hence, there is no amplification of the electromagnetic field.

It should be noted that the coefficient of electromagnetic wave absorption in the subterahertz frequency range depends on the substrate parameters. In Fig. 13, the frequency dependences of L_ω are shown for two samples with identical parameters of their active elements, but different substrate thicknesses. If the substrate thickness $d_s = 0.036$ cm, the frequency window of DNDM does not coincide with any of the frequencies ω_r of Fabry–Perot modes. At such non-resonance parameters, the values of $|L_\omega|$ and, hence, the amplification of the electromagnetic field are substantially lower than those in the resonance case where $d_s = 0.04$ cm. Therefore, we may say about a selective role of the substrate in the amplification of the electromagnetic field in the subterahertz frequency range.

In experiments dealing with the transmission of radiation through semiconductor structures, it is much more convenient to measure the transmission coefficient at a given frequency by varying the amplitude of the applied dc field. In Fig. 14, *a*, the dependences of DDM on the applied field amplitude obtained in the parallel, μ_E^\parallel , and transverse, μ_E^\perp , field configurations at a frequency of 0.64 THz are shown. The real and imaginary parts of μ_E^\parallel have an oscillatory behavior, and the DNDM is realized in a narrow interval of dc fields with the amplitudes of about 3 kV/cm. At the same time, the real and imaginary parts of μ_E^\perp almost do not change at that. At a frequency of 0.64 THz, a substantial difference between μ_E^\parallel and μ_E^\perp is observed starting from the applied field values of 2–3 kV/cm.

Experimentally, it is possible to observe the field-induced difference between the transmission coeffi-

cients for electromagnetic waves with polarizations along, $T_{\parallel,E}$, and across, $T_{\perp,E}$, the dc field. In Fig. 14, *b*, the bold and thin curves illustrate the field dependence for $T_{\parallel,E}$ and $T_{\perp,E}$, respectively. A monochromatic beam, which initially was not polarized, after having passed through the sample, became partially polarized. The polarization degree of such a beam, P_E , depends on the dc field amplitude, as is shown in Fig. 14, *c*. The quantity P_E is defined as follows: $P_E = (T_{\parallel,E} - T_{\perp,E}) / (T_{\parallel,E} + T_{\perp,E})$. From Fig. 14, *c*, one can see that the behavior of P_E reproduces the oscillatory dependence of DDM μ_E^\parallel on the field, which points to the formation of the streaming and the appearance of the OPTTR. Beyond the range of resonance fields, the value of P_E monotonously grows, and the oscillations are absent, which means that the system is not in the OPTTR. Such a specific dependence of the degree of polarization of the electromagnetic wave that passed through the sample on the electric field may also be a characteristic feature of the OPTTR.

6. Conclusions

To summarize, the calculations of the stationary and high-frequency characteristics of compensated GaN are carried out, which were aimed at revealing the typical features of the streaming effect and the conditions needed for the effect to emerge. In particular, it is found that a strongly anisotropic distribution of electrons appears in GaN with an impurity concentration of 10^{16} cm $^{-3}$ and an electron concentration of 10^{15} cm $^{-3}$ in the range of applied electric fields 3–8 kV/cm and the temperature interval 30–150 K. Such a distribution manifests itself as a characteristic saturation in the dependences of the drift velocity and the total average energy of electrons on the field. The dependence of the transverse diffusion coefficient on the field decreases until it reaches the characteristic saturation. In the framework of the low-signal response approximation, the spectra of the high-frequency electron mobility are obtained in the parallel and perpendicular configurations of the stationary and high-frequency fields. It is shown that, in the case of the parallel configuration, there exists a transit-time resonance effect in the frequency range 0.5–2 THz and the field range 2–10 kV/cm, and the negative dynamic differential mobility can arise. In the perpendicular configuration, the negative dynamic differential mobility does not arise, and

the spectrum of the dynamic mobility is close to the Drude–Lorentzian shape.

On the basis of aforementioned calculations, a theory is developed for the transmission of terahertz radiation through a structure with an epitaxial GaN layer. The relative coefficient of terahertz radiation amplification by the structure operating in the transit-time resonance regime is calculated. For a single passage of the wave through the GaN structure, the maximum of the relative amplification coefficient is equal to 1.5%, which is three times as large as the losses obtained at the reflection of the same wave from metallic mirrors. It is shown that the anisotropy of the dynamic mobility leads to a dependence of the transmission coefficients on the incident wave polarization. The polarization degree of the wave that passed through the structure can be controlled by changing the magnitude of applied electric field.

The authors are sincerely grateful to Prof. V.O. Kochelap (Institute of Semiconductor Physics, National Academy of Sciences of Ukraine, Kyiv) and Prof. L. Varani (Montpellier University, France) for their interest in our researches and their active participation in the discussion of various aspects of this work. The calculations were carried out, by using a computer cluster at the Institute of Semiconductor Physics (Kyiv) in the framework of the State goal-oriented scientific and engineering program on introducing grid technologies for 2009–2013.

1. W. Shockley, *Bell Syst. Tech. J.* **30**, 990 (1951).
2. I.M. Dykman and P.M. Tomchuk, *Transport Phenomena and Fluctuations in Semiconductors* (Naukova Dumka, Kyiv, 1981) (in Russian).
3. D.K. Ferry, *Semiconductors* (Macmillan, New York, 1991), Ch. 10.
4. V.E. Gantmakher and Y.B. Levinson, *Carrier Scattering in Metals and Semiconductors* (North-Holland, Amsterdam, 1987).
5. G.A. Baraff, *Phys. Rev.* **128**, 2507 (1962); *Phys. Rev. A* **133**, 26 (1964).
6. E. Vasilyus and E. Levinson, *Zh. Eksp. Teor. Fiz.* **50**, 1660 (1966); **52**, 1013 (1967).
7. Z.S. Gribnikov and V.A. Kochelap, *Zh. Eksp. Teor. Fiz.* **58**, 1046 (1970).
8. W. Cox, *J. Phys. Condens. Matter* **2**, 4849 (1990).
9. W. Fawcett, A.D. Boardman, and S. Swain, *J. Chem. Solids* **31**, 1963 (1970).
10. C. Jacoboni and L. Reggiani, *Rev. Mod. Phys.* **55**, 645 (1983).
11. A. Matulionis, J. Pozela, and A. Reklaitis, *Phys. Status Solidi A* **31**, 83 (1975).
12. R.C. Curby and D.K. Ferry, *Phys. Status Solidi A* **20**, 569 (1973).
13. F.M. Peeters, W. Van Puymbroeck, and J.T. Devreese, *Phys. Rev. B* **31**, 5322 (1985).
14. T.W. Hickmott, P.M. Solomon, F.F. Fang, F. Stern, R. Fischer, and H. Morkos, *Phys. Rev. Lett.* **52**, 2053 (1984).
15. P-F Lu, D.C. Tsui, and H.M. Cox, *Phys. Rev. B* **35**, 9659 (1987).
16. C.B. Hanna, E.S. Hellman, and R.B. Laughlin, *Phys. Rev B* **34**, 5475 (1986).
17. M. Levinstein, S. Rumyantsev, and M. Shur, *Properties of Advanced Semiconductor Materials: GaN, AlN, InN, BN, SiC, SiGe* (Wiley, New York, 2001).
18. A.A. Andronov and V.A. Kozlov, *Pis'ma Zh. Eksp. Teor. Fiz.* **17**, 124 (1973).
19. Ya.I. Alber, A.A. Andronov, V.A. Valov, V.A. Kozlov, A.M. Lerner, and I.P. Ryazantseva, *Zh. Èksp. Teor. Fiz.* **72**, 1031 (1977).
20. L.E. Vorob'ev, S.N. Danilov, V.N. Tulupenko, and D.A. Firsov, *JETP Lett.* **73**, 219 (2001).
21. N. Ishida and T. Kurosawa, *Jpn. J. Appl. Phys.* **64**, 2994 (1995).
22. P.N. Shiktorov, *Sov. Phys. – Collect.* **25**, 59 (1985).
23. V.A. Kozlov, A.V. Nikolaev, and A.V. Samokhvalov, *Semicond. Sci. Technol.* **19**, s99 (2004); E. Starikov, P. Shiktorov, V. Gruzinskis, L. Varani, C. Palermo, J.-F. Millithaler, and L. Reggiani, *J. Phys. Condens. Matter* **20**, 1 (2008).
24. E.A. Barry, K.W. Kim, and V.A. Kochelap, *Phys. Status Solidi B* **228**, 571 (2001); *Appl. Phys. Lett.* **80**, 2317 (2002).
25. V.M. Polyakov and F. Schwierz, *J. Appl. Phys.* **100**, 103704 (2006).
26. V.V. Korotyeyev, G.I. Syngayivska, V.A. Kochelap, and A.A. Klimov, *Semicond. Phys. Quant. Electr. Optoelectr.* **12**, 328 (2009).
27. E. Starikov, P. Shiktorov, V. Gruzinskis, L. Reggiani, L. Varani, J.C. Vaissiere, and J.H. Zhao, *J. Appl. Phys.* **89**, 1161 (2001).
28. E. Starikov, P. Shiktorov, V. Gruzinskis, L. Regiani, L. Varani, J.C. Vaissiere, and J.H. Zhao, *IEEE Trans. Electron Devices* **48**, 438 (2001); *Phys. Status Solidi A* **198**, 247 (2002).
29. E. Starikov, P. Shiktorov, V. Gruzinskis, L. Varani, C. Palermo, J.-F. Millithaler, and L. Regiani, *J. Phys. Condens. Matter* **20**, 384209 (2008); *Phys. Rev. B* **76**, 045333 (2007).
30. J.T. Lu and J.C. Cao, *Semicond. Sci. Technol.* **20**, 829 (2005).
31. V.V. Korotyeyev, V.A. Kochelap, K.W. Kim, and D.L. Woolard, *Appl. Phys. Lett.* **82**, 2643 (2003).
32. K.W. Kim, V.V. Korotyeyev, V.A. Kochelap, A.A. Klimov, and D.L. Woolard, *J. Appl. Phys.* **96**, 6488 (2004).

33. J.T. Lu, J.C. Cao, and S.L. Feng, *Phys. Rev. B* **73**, 195326 (2006).
34. V.N. Sokolov, K.W. Kim, V.A. Kochelap, and D.L. Woolard, *Appl. Phys. Lett.* **84**, 3630 (2002).
35. V.V. Mitin, V.A. Kochelap, and M. Stroschio, *Quantum Heterostructures for Microelectronics and Optoelectronics* (Cambridge Univ. Press, New York, 1999).
36. V.L. Bonch-Bruевич and S.G. Kalashnikov, *Semiconductor Physics* (Nauka, Moscow, 1977) (in Russian).
37. M.S. Gupta, *J. Appl. Phys.* **49**, 2837 (1978); R. Fauquembergue, J. Zimmermann, A. Kaszynski, and E. Constant, *J. Appl. Phys.* **51**, 1065 (1980).
38. M.A. Littlejohn, J.R. Hauser, and T.H. Glisson, *Appl. Phys. Lett.* **26**, 625 (1975).
39. D.C. Look and J.R. Sizelove, *Appl. Phys. Lett.* **79**, 1133 (2001).
40. L. Bouguen, S. Contreras, B. Jouault, L. Konczewicz, J. Camassel, Y. Cordier, M. Azize, S. Chenot, and N. Baron, *Appl. Phys. Lett.* **92**, 043504 (2008).
41. V. Bareikis, A. Matulionis, J. Požela, S. Ašmontas, A. Reklaitis, A. Galdikas, R. Miliušytė, and E. Starikovas, *Hot Electron Diffusion* (Mokslas, Vilnius, 1981) (in Russian).
42. E. Starikov, P. Shiktorov, V. Gruzinskis, L. Reggiani, L. Varani, J.C. Vaissiere, and C. Palermo, *Semicond. Sci. Technol.* **20**, 279 (2005).
43. D.J. Bartelink and G. Perski, *Appl. Phys. Lett.* **16**, 191 (1970).
44. J. Zimmermann, Y. Leroy, and E. Constant, *J. Appl. Phys.* **49**, 3378 (1978).
45. P.A. Lebowl, *J. Appl. Phys.* **44**, 1744 (1973).
46. T. Laurent, R. Sharma, J. Torres, P. Nouvel, S. Blin, L. Varani, Y. Cordier, M. Chmielowska, S. Chenot, J.-P. Faurie, B. Beaumont, P. Shiktorov, E. Starikov, V. Gruzinskis, V.V. Korotyeyev, and V.A. Kochelap, *Appl. Phys. Lett.* **99**, 082101 (2011).

Received 14.02.12.

Translated from Ukrainian by O.I. Voitenko

Г.І. Сунгаївська, В.В. Коротеєв

ЕЛЕКТРИЧНІ ТА ВИСОКОЧАСТОТНІ ВЛАСТИВОСТІ КОМПЕНСОВАНОГО GaN В УМОВАХ ЕЛЕКТРОННОГО СТРИМІНГУ

Резюме

Проведено детальний аналіз умов існування стримінгу і ефекта прольотного резонансу на оптичних фонах у компенсованому об'ємному GaN. Методом Монте-Карло проведено розрахунки високочастотної диференціальної рухливості. Показано, що при низьких температурах ґратки 30–77 К в електричних полях 3–10 кВ/см в терагерцовому діапазоні частот може існувати динамічна від'ємна диференціальна рухливість. Виявлені нові ознаки ефекту стримінгу – анізотропія динамічної диференціальної рухливості і особлива поведінка коефіцієнта дифузії у перпендикулярному до постійного електричного поля напрямку. Побудовано теорію проходження терагерцового випромінювання через структуру з епітаксійним шаром GaN. Отримано умови підсилення електромагнітних хвиль в діапазоні частот 0,5–2 ТГц. В електричних полях, більших, ніж 1 кВ/см, спостерігається поляризаційна залежність коефіцієнта проходження випромінювання через структуру.